Numerical Analysis of Multihole Gasoline Direct Injection Sprays

M. M. Khan[1*], J. Helie[*], M. Gorokhovski[†], A. Wood[+], G. Wigley[+], J. Kashdan[‡], J. P. Dumas[‡], M. Mojtabi[**], P. Guibert[**]
* Continental Automotive SAS, BP 1149 Toulouse Cedex 1, France
[†] Ecole Centrale de Lyon, Lyon, France, [+]Loughborough Universty, Leicestershire, UK
[‡]IFP Énergies nouvelles, 1-4 avenue de Bois Préau, 92852 Rueil Malmaison, France,
[**] Université Pierre et Marie Curie, Paris France
[1]Muhammad.2.Khan@continental-corporation.com

Abstract

Multi-hole gasoline direct injection (GDI) injector sprays have been studied numerically and experimentally. This study is an extension of previous work performed by Rossella Rotondi [1]. The main part of this work focuses on air entrainment and droplet size prediction in the spray plumes under non-evaporating and evaporating conditions, which can have a significant effect on jet to jet interactions, spray propagation and mixture formation. For this purpose, several Continental's special XL gasoline direct injector geometries have been studied including a 3-hole 90° Cone Angle (CA) and 6-hole 60° CA injectors. The droplet size distributions of 3-hole injector under non-evaporating conditions show sufficient droplets' breakup. Spray penetrations and the air entrainment fields of 3-hole and 6-hole injectors from simulation and experiments under evaporating conditions are quite comparable. Furthermore, the vapour and the air entrainment fields of the 6-hole spray suggest that the vapour is accumulated in the central region of the spray because the air entrained near the nozzle region is pushed downstream. The air pushed at the tips of the plumes is entrained inside the spray cone and it counters the downstream motion of the gas at a certain location. This generates a stagnation point and produces a radial flow which forces the spray plumes to bend from their original path.

Introduction

A typical advantage of a multi-hole GDI injector is to increase the fuel efficiency by reducing fuel injection timing, penetration and increasing the fuel-air mixture quality with sufficient vapor homogeneity for better combustion in the engines. These goals are only possible if the intended spray cone angle, desired spray plumes' path and optimum atomization of the droplets are achieved [2]. But since in multi-hole GDI injectors mostly jet to jet interactions are present which make these tasks very difficult to be fulfilled and thus cause the spray to miss the intended targeting or sometimes even make the spray collapse under certain conditions. To avoid these spray plume interactions a deep understanding of the air entrainment of the spray plumes needs to be developed.

Multi-hole GDI injectors have been studied in some detail in [1] in terms of spray plume angle variations and droplet sizing. The effects of gas entrainment on the mixture formation of GDI hollow cone injector sprays under various injection pressures have been investigated experimentally using Particle Image Velocimetry (PIV) in [3]. Another interesting experimental investigation using PIV was performed in order to study air entrainment variations induced by injection fluctuations in [4]. Numerical and experimental analysis of a GDI annular orifice spray with the effects of air entrainment on the spray structures has been done in [5]. Multi-hole evaporating sprays were studied experimentally in [6] which revealed the air entrainment and vapor accumulation inside the cone but did not enable an explanation of the phenomena of air entrainment and its effects on spray behavior.

Therefore in order to gain a more detailed insight into the performance of multi-hole GDI injectors, Phase Doppler Anemometry (PDA) measurements of droplet sizes were performed by Loughborough University under non-evaporating conditions for the 3-hole nozzle. Also high-speed (Mie scattering) imaging of the liquid phase and PIV measurements were performed at IFP Energies Nouvelles (IFPEN) in order to quantify the spray development and air entrainment characteristics respectively for both the 3 and 6-hole injectors in evaporating conditions. Experimentally it proved particularly challenging to perform air entrainment measurements on the 6-hole nozzle due to its narrow cone angle. The high droplet concentrations between adjacent plumes resulted in significant laser elastic and multiple scattering effects. For such complicated nozzle geometries, numerical studies are therefore particularly useful.

1. Experimental setup and operating conditions:

The experimental setups used to perform the PDA measurements and PIV measurements are described below:

* Corresponding author: Muhammad.2.Khan@continental-corporation.com

1.1 Experimental set-up of PDA test bench:

The design, construction and application of the Loughborough University two component PDA transmission system to study dense GDI fuel sprays has been well documented [7] and the configuration has been kept constant from previous experiments (reference to my ILASS 2011 paper).

The three-hole GDI injector was supported from a gantry incorporating a rotation stage and three precision orthogonal linear traverses to orientate and position the spray in three dimensions relative to the static PDA measurement volume. Each radial scan started from the geometric vertical axis through the nozzle tip and traversed out to the periphery of the spray stream. The measurement co-ordinates in the vertical plane were Z = 10, 20, 30, 40, 50 and 60 mm below the nozzle tip. The horizontal traverse was computer controlled and programmed with a radial step increment of nominally 7 - 10% of the Z value in order to resolve local high velocity gradients across the cone of the spray stream in the horizontal plane.

1.2 Experimental set-up of PIV test bench:

PIV measurements and high-speed spray (Mie scattering) imaging were performed by IFPEN in the high pressure, high temperature constant volume chamber [8, 9, 10]. The chamber has a total volume of 1.4 L (112 mm x 112 mm) and is capable of reproducing the high pressure (0-150 bar) and high temperature (293- 1000 K) conditions that are encountered in gasoline and diesel internal combustion engines. The chamber is equipped in such a way as to enable accurate control of the ambient pressure and temperature conditions. The injector fuel temperature and nozzle temperature are also controlled by specific cooling circuits. The test cell includes five 70 mm diameter sapphire windows providing significant optical access for the application of laser diagnostic techniques.

Two Continental XL gasoline direct injectors were studied including a 3-hole 90° CA nozzle and a 6-hole 60° CA nozzle. The injectors were mounted in such a way that the measurement plane is between the two jets. The 3-hole injector was inclined at an angle of 35° with respect to the z-axis in order to separate the two spray plumes from the third plume which is positioned in the middle and further behind the other two plumes. In a similar manner, two plumes from the 6-hole nozzle were studied by inclining the injector at an angle of 35° with respect to the z-axis. The light source used for the PIV experiments was a PIV 400 Spectra Physics laser. The double cavity of the laser generates two pulsed beams with the energy of 200mJ each at a wavelength of 532nm. The laser frequency was 10 Hz and the two laser pulses were separated by a time delay (Δt) which was adapted according to the measured velocity range (the Δt value typically used in this study was 20 μs). The laser beams were transformed into a 2D laser sheet by diverging and converging lenses. In order to align the PIV measurement plane in between the two jets, a laser sheet entered the test cell through a sapphire window in the base of the chamber by using a 45° mirror. The laser sheet illuminated a vertical plane in the chamber between the floor of the chamber and the chamber roof in the direction of the injector tip.

1.3 Operating conditions:

The operating conditions for both the XL 3-hole 90° CA and XL 6-hole 60° CA injectors are presented in the table below:

Conditions and Experiment type	Injectors	Injection Pressure (P_i) (bar)	Fuel Temperature (T_f) (°C)	Chamber Pressure (P_c) (bar)	Chamber Temperature (T_c) (°C)	Injection Duration (ms)	Total Injected Mass (mg)	Fuel Type
Non-evaporating-PDA	3-hole	100	20	1	20	2.0	15	Gasoline
Evaporating-PIV	3-hole	200	90	1.54	33	3.32	24.9	Iso-Octane
Evaporating-PIV	6-hole	200	90	1.54	33	3.387	49.8	Iso-Octane

Table 1: Operating conditions of experiments (PDA and PIV) and Simulations

.

2. Numerical simulation setup:

The Reynolds Average Navier Stokes (RANS) simulations were performed on OpenFOAM ® [11] version 1.7.1, where the gaseous phase was modeled by the standard K-Epsilon approach and the liquid phase was modeled by the Lagrangian approach. A compressible reacting spray solver based on the standard dieselFoam solver and automatic mesh refinement (AMR) of interDyMFoam was used. This solver was implemented in OpenFOAM ® with the help of [12] which gives the solver a capability of AMR. The PISO (pressure implicit with splitting off operators) algorithm [13] was implied with 2 iterations of the PISO loop for the predictor correction. A second order setup for the space discretization and first order setup for time discretization was utilized. Gauss limited linear scheme which is a second order bounded scheme, was employed for the divergence scheme. Gauss

linear corrected scheme, a second order unbounded conservative laplacian scheme was used. Euler Implicit scheme, first order accurate in time which depends on the courant number for the stability was chosen for the time discretization. Automatic time step adjustment was also included to keep local courant number to be less than 0.5 with initial time step of 10^{-7} sec. Preconditioned bi-conjugate gradient method [14] with Diagonal in-complete-Cholesky (symmetric) preconditioner (DIC) for pressure equation and Diagonal incomplete-LU (asymmetric) for the equations of the rest of the quantities like velocity, kinetic energy etc were used with a local accuracy of 10^{-7} at every time step.

A computational domain of size 112 mm x 112 mm x 112mm with an initial cell size of 1.5 mm was used for the simulations with a mesh refinement interval of 2 and maximum cell limit of 5 million. The initial cell size after being refined twice reduced to a minimum cell size of 0.375 mm. Maximum limit of cells ensures the cell size doesn't increase beyond the computational resources. AMR was based on the scalar fields of kinetic energy and vapour mass fraction for non-evaporating and evaporating conditions, respectively.

2.1 Spray models:

A spray is sometimes referred to as a cluster of small droplets moving at high velocity in a continuum because when a pressurized liquid jet enters a gaseous environment it exchanges momentum with the slow moving or quiescent gas and thus causes breakup of the liquid jet into smaller droplets. Therefore for high pressure cases blob injection is preferred for the fuel injection which eliminates the need of a primary atomization model and requires only the use of a secondary atomization model. As the spray plume moves further downstream the effect of drag, inter-droplet collisions, evaporation and heat transfer become prominent and the spray becomes more complex to predict and model. One of the most important features of the sprays is the air entrainment rate which has a main influence on the motion of the droplets. Therefore several sub models need to be included in spray modeling. The library of OpenFOAM covers large number of different spray sub-models which had been used in the simulations.

2.1.1 Blob injection model:

A Rosin Rammler droplet distribution function was utilized for the blob injection with 12° angle for each of the spray plumes was assumed. The coefficients of Rosin Rammler distribution used in the simulations were n= 3, d= 100 µm and 1µm < x< 150µm.

2.1.2 Droplet breakup model:

For the secondary atomization Enhanced TAB (Taylor Analogy Breakup) was used. The ETAB model uses the same concept of droplet deformation as a standard TAB model but with different relations for the breakup of parent droplet to child droplets [15]. The relationship of child droplet radius (*Rc*) to parent droplet radius (*Rp*) relationship is given below as:

$$R_c/R_p = e^{-K_{br}t} \;;\; where\;\; K_{br} = \begin{cases} k_1 w & We \le We_t \\ k_2 w\sqrt{We} & We > We_t \end{cases} \qquad (1)$$

K_{br} is a constant depending on the regime of droplet breakup. There are two droplet breakup regimes which can occur i.e. either bag breakup or stripping breakup. k_1 and k_2 are the constants which was set to 0.2 and We_t is the transition Weber number which distinguishes the two regimes and was set to 100 for all cases.

2.1.3 Dispersion, collision, evaporation and drag models:

Droplet dispersion is caused by the turbulent gas motion. A stochastic dispersion model which is based on [16] was used in the simulation. It uses the turbulence correlation time relationship from [17].

Trajectory model of Nordin [18] was utilized in the simulations, which is based on the O'Rourke collision model [19] with some modifications.

The evaporation model is based on simple D^2 law and it uses the Sherwood number calculated from Ranz-Marshal correlation to calculate evaporation relaxation time. This model is well explained in [20].

As the droplets move downstream they experience drag force which slows down these droplets. In order to incorporate drag force in the spray simulation standard drag law with the values based on the coefficient of drag (C_d) and the value of droplet Reynolds number (Re) was used.

3. Results and discussion:

The results are discussed below for both non-evaporating and evaporating conditions in detail.

3.1 Non-evaporating conditions:

The simulation results of droplet size distributions of 3-hole injectors are compared with experimental PDA results, under non-evaporating conditions presented in the table 1. The plot in figure 1 (left) shows a comparison between the simulation and experimental results for the average droplets size (D_{10}) at different axial locations at the centre of a single plume for a time interval of 1.6 to 2ms. The mean droplet sizes at 10 mm downstream location at the centre of the plumes are 7.55µm and 7.43 µm for the experiment and simulation respectively. The mean droplet size reduces to 5.89 µm at 40 mm location in the experiments where as in simulation it is 6.55 µm in figure 1 (right). The probability density function (PDF) of droplet size distribution at 40 mm downstream location at the centre of a single separated plume also show good agreement.

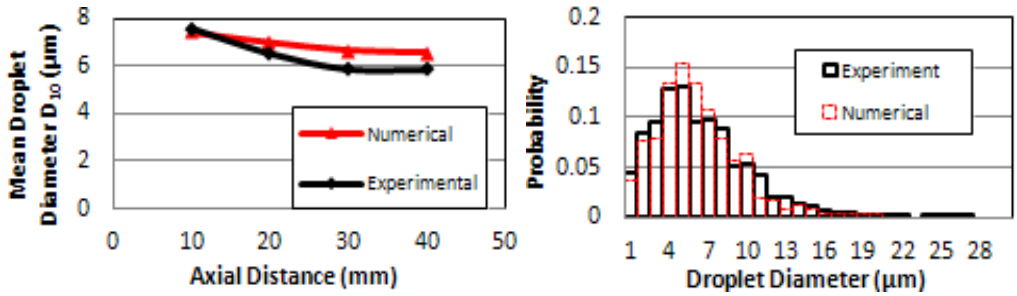

Fig 1: Experimental and simulation results of 3-hole injector; Mean droplet diameter (D_{10}) at different axial locations (left), PDF of droplet distribution at 40 mm axial location (right)

3.2 Evaporating conditions:

3.2.1 Axial liquid penetration of the spray:

Axial liquid penetration rates of the spray are compared for both the 3-hole and 6-hole injectors experimentally and numerically under evaporating conditions listed in table 1. The results in figure 2 reveal that both injectors have similar penetration rates despite the fact that the nominal nozzle geometries differ significantly between the two injectors. The numerical prediction of the global spray penetration is comparable with the experimental data. A delay of 400 µs was observed for the experiments between the electrical start (injector trigger) and the physical start of injection (first appearance of liquid at the nozzle exit). This delay incorporates the electrical delay (solenoid activation) and hydraulic delay (internal nozzle fluid flow). This delay is also included in the simulations to have the same starting time of fuel injection.

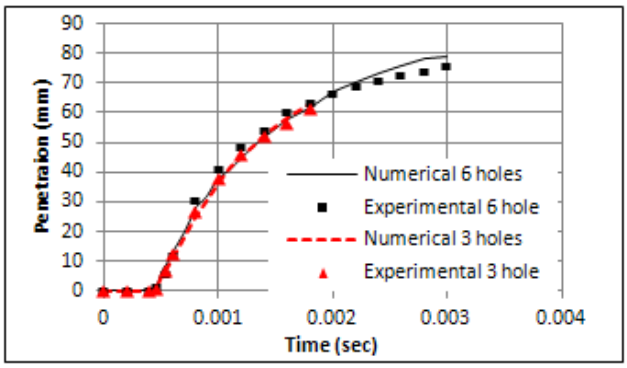

Fig 2: Comparison of penetration curves under evaporating conditions for 3 and 6-hole injectors

3.2.2 Air entrainment between the two jets:

A comparison of the 2D flow fields measured experimentally and simulated numerically under the evaporating conditions has been presented below. The air entrainment characteristics for the 3-hole and 6-hole injectors are shown in figures 3 on top and bottom respectively, at a time 1.4 ms *After Start Of Injection* (ASOI). In both cases the numerical results show satisfactory agreement with the experimental data. The air entrainment is relatively high in the near nozzle region and at the spray tip leading edge as a result of the high spray momentum for both the 3 and 6-hole injectors.

On the contrary, the 6-hole injector reveals a quite different structure. Experimental measurements show that the spray collapses compared to the 3-hole injector. The spray collapse is believed to be linked to the more significant jet-jet interactions which modify the air entrainment characteristics. Unfortunately PIV data could not be acquired in the inter-jet spacing for the 6-hole injector due to spray collapse and the resulting formation of what appears to be a continuous spray plume. The air entrainment in between the jets is discussed in more detail in the section entitled “jet to jet interactions”. The resulting difference between the experimental and computational

results as shown on figure 3 (top left, bottom left) does not exceed 2.5m/s and mostly the error appears to be local or linked to the main direction of the flow more than the absolute value i.e. the error vectors are mainly perpendicular to the main direction from experimental.

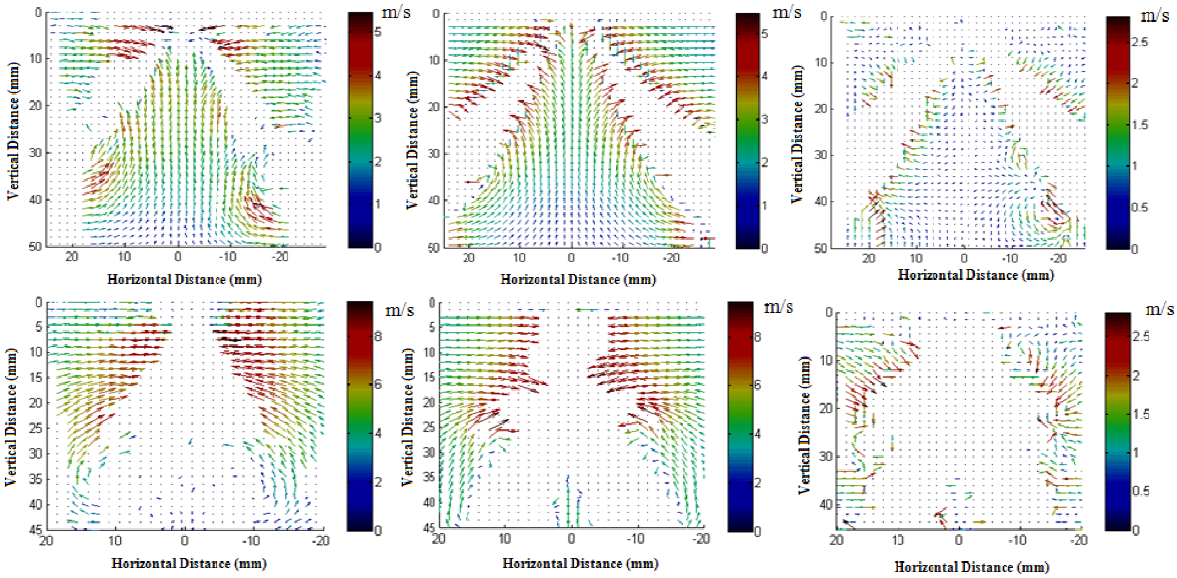

Fig 3: 2D vector flow fields showing air entrainment at 1.4ms ASOI for the 3-hole injector (top row) and 6-hole injector (bottom row); Experimental (left), Simulation (middle), Difference between Experimental & Simulated results (right)

3.2.3 Jet to jet interactions:

Jet to jet interactions can be significant for multi-hole injectors and as a result have an effect on the global spray structure. The simulation results obtained for the 6-hole injector under the evaporating conditions presented in table 1, reveals the presence of what appear to be jet to jet interactions causing a modification in terms of the trajectory of the individual spray plumes as shown in figure 4. In contrast, the spray plumes are well separated in the case of the 3-hole injector. However, the 6-hole injector reveals a continuous spray structure, due to the presence of droplets and it becomes difficult to identify individual plumes. One would expect that significant interactions occur between adjacent jets, modifying the air entrainment and subsequently the fuel-air mixture distribution. Such aspects are studied in more detail by performing numerical simulations.

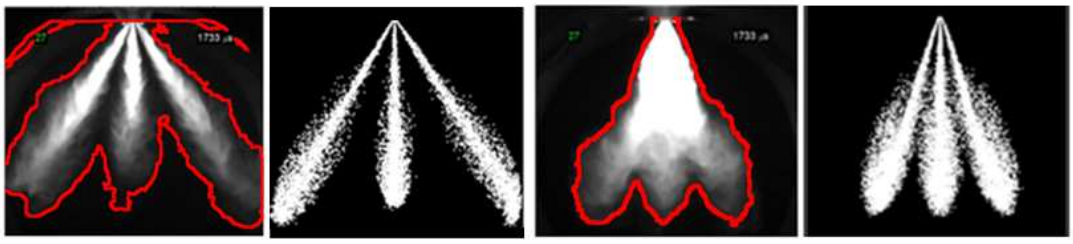

Fig 4: Liquid phase spray images of the sprays under evaporating conditions at 1.75ms ASOI; (From Left): Experimental result (high-speed Mie scattering) of 3-hole injector, Simulation result of 3-hole injector, experimental result (high-speed Mie scattering) of 6-hole injector, Simulation result of 6-hole injector

3.2.3.1 Spatial evolution of vapour phase:

The simulation results of the vapour phase of 6-hole injector under evaporating conditions provide further insight to the process involved in the spray propagation, structure and mixture formation. A sequence of images containing various cross-sectional planes of the vapor mass fraction along the axial direction of the spray plumes is presented below in figure 5 at time step of 3.10ms ASOI. The cross-sections near the nozzle spray region reveal a star shape of the spray plumes which are well separated from one another. The images also divulge vapor phase fuel in the central region of the spray. Moving further downstream the vapor phase fuel surrounding the plumes tends to merge into one other. At this point the star shape transforms into a closed ring structure and the spray reveals a hollow cone spray structure. It is at this stage where the spray plumes tend to deflect resulting in a notable change in spray angle. This process takes places throughout the spray propagation. In order to better understand the observed behavior, an analysis of the air entrainment characteristics has been performed.

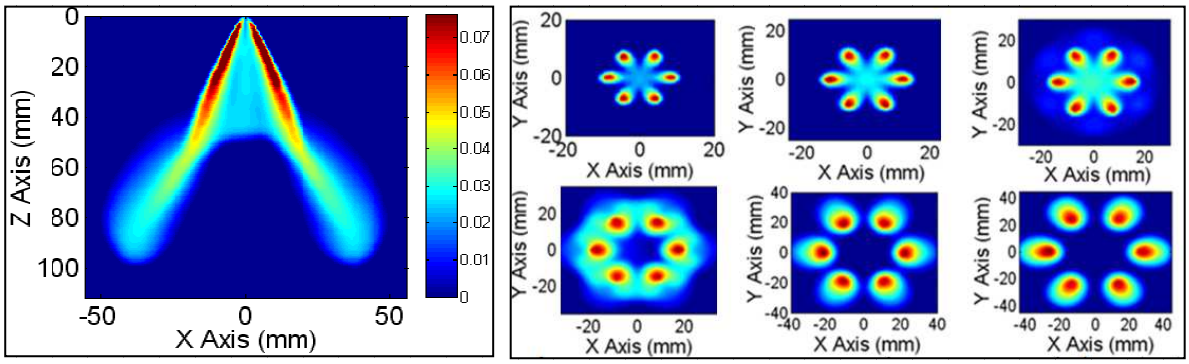

Fig 5: Simulation results of fuel vapor mass fraction at 3.1 ms ASOI, 2D axial cross-sectional plane (x, z) (left), 2D horizontal cross-sectional planes (x, y) (right): with 20mm (top left), 30mm (top middle), 40mm (top right) 50mm (bottom left), 60mm (bottom middle), 70mm (bottom left)

3.2.3.2 Axial gas velocity:

The gas entrainment between two adjacent plumes (vertical cross-sections (x-z)) of 6-hole injector at 1.75ms and 3.10ms ASOI is presented in figure 6. Typically gas entrainment into the spray plumes can be divided into two sections (1) air sucked into the near nozzle region and (2) air and vapor pushed downwards in the direction of the spray at the spray tip [3, 6]. These two phenomena can be observed with vapor being sucked in towards the injector tip and pushed out at the spray tip as shown in figure 6.

A new feature is also revealed, whereby air between the two jets is pushed downwards in the upper half of the spray cone (close to the injector tip). This is usually not observed in the sprays with spatially well separated plumes and wide cone angles as is the case for the 3-hole injector with results shown in figure 6.

The internal downward gas flow in the upper half of the spray cone encounters an inverse flow, originating from the lower downstream region of the spray which is the usual internal air entrainment. When the two flows hit each other at 30 mm at 1.75 ms and 50 mm at 3.10 ms, they form a stagnation plane resulting in a very high radial flow toward the external side as seen in the figure 6. This radial flow forces the spray plumes to deviate suddenly from their original paths with a noticeable change in the angles. In our operational conditions, the collapsing tendency then vanishes here and the plumes separated from each other which can be seen in figure 5.

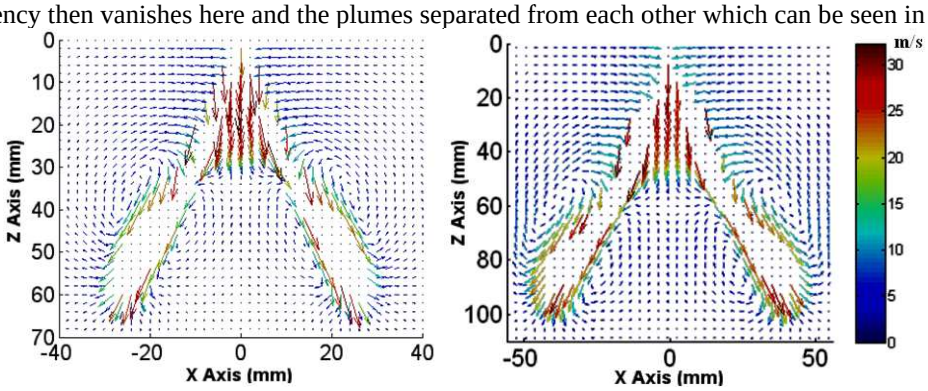

Fig 6: 2D velocity vector plots of simulated air and gas entrainment; 1.75ms ASOI (left), 3.10 ms ASOI (right)

However, a second difference observed on the 6-hole compared to 3-holes is on bottom half part of the spray cone (far away from the injector needle). Here the spray tip recirculation area is strongly reduced in its central part. This reduction is approximately compensated by an increased recirculation area on the external side. This asymmetry external/internal is observed where the jet plumes are widely separated.

3.2.3.3 Comparison of spray angles:

A modification of the global spray angle was observed experimentally from high-speed spray imaging performed in the HPHT chamber at IFPEN on the XL 6-hole 60° CA injector. The simulation and experimental data is shown in figure 7 on left and right respectively, for this particular case. The spray cone can be divided into two regions corresponding firstly, to a close-up, near nozzle zone and secondly, to a downstream region where one observes a modification of the spray angle as shown in figure 7 (left). The angles are measured by capturing images of the simulated spray in the y-z plane. These spray images at two time steps corresponding to 1.75 and 3.10 ms ASOI are analysed by "imageJ" software which is a simple java based image processing. The angle of the near nozzle zone (α_c) at 1.75 ms and at 3.10 ms ASOI is approximately 42°.

These near nozzle angles suggest that the measured spray cone angle is in fact narrower than the nominal cone angle of 60°. The near angles are measured from plume centre to plume centre which implies that taking

account of the half plume angle (6°) of each of the two spray plumes, the total cone angle will be approximately 54°. A difference of approximately 6° between the nominal angle and the measured, near nozzle angle indicates the spray collapse in the close up (upper) region. In the downstream zone of the spray, at 1.75 ms ASOI, the deflected spray angle (α_d) is approximately 48° which increases to 51° at 3.10 ms ASOI. The spray cone is thus deflected by 6 ° and 9 ° at 1.75 ms and 3.10 ms ASOI respectively. Although the spray far cone angles (α_f) of both experimental and numerical results show very good agreement but the spray plumes propagate with two different angles near and far from the injector nozzle. That means the overall spray cone angle is not a pure indicator of the spray directions when there are strong jet to jet interactions present.

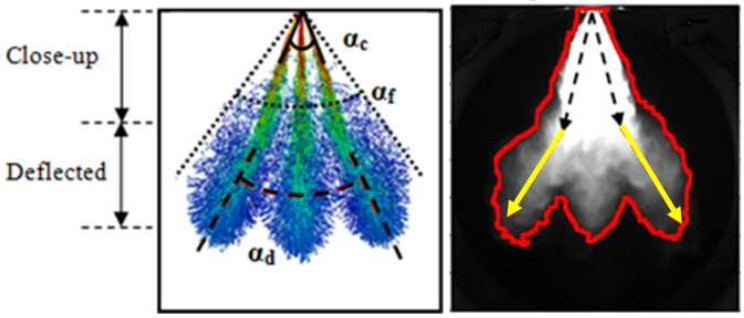

Fig 7: Comparison of spray plumes at 1.8 ms ASOI; Simulation result (left), experimental result (right)

Time (ms)	Simulated Close up Angle (α_c)	Simulated Deflected Part Angle (α_d)	Simulated Far cone angle (α_f)	Experimental Far cone angle (α_f)
1.75	42°	48°	66°	65°
3.10	42°	51°	65°	65°

Table 2: Angles of close-up and deflected part of the spray at time 1.75 ms and 3.10 ms

3.2.3.4 Radial gas velocity:

Horizontal planes showing radial velocity vector plots of air entrainment at different axial locations at 3.10 ms ASOI are shown in figure 8. The vector plots show that until 40mm downstream air is sucked from the outer region and pushed out afterwards. The air entrainment in the inner side of the spray plumes infect comes from the accelerating flow in between the jets. A part of the air movement in between the jets which misses its target is pushed downstream because there is almost no time for this air to turn towards the plumes due to the high speed of spray plumes.

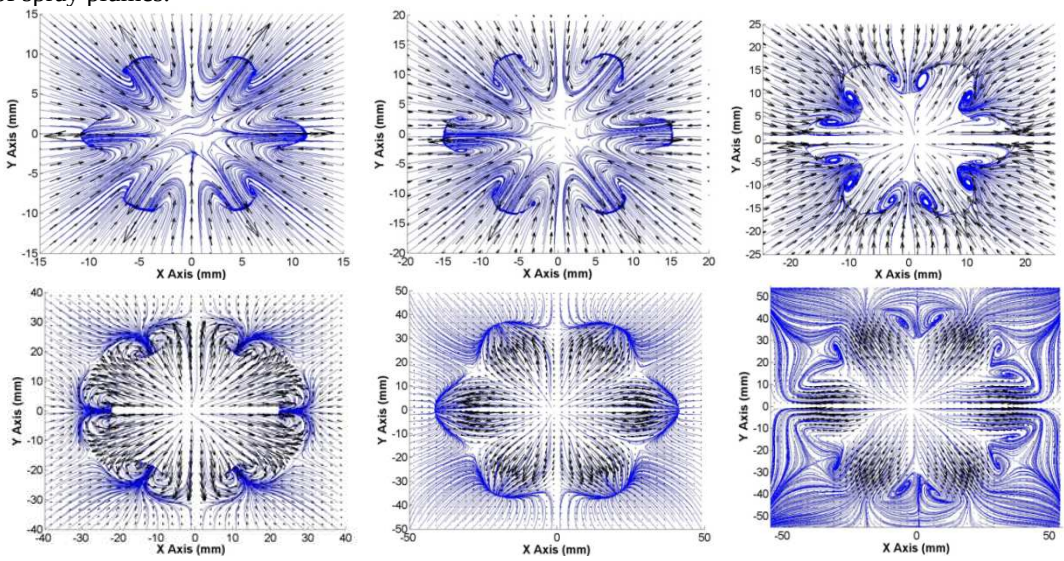

Fig 8: Radial velocity vector plot of the simulated air entrainments at 3.10ms ASOI at downstream locations; 20mm (top left), 30mm (top middle), 40mm (top right), 50mm (bottom left), 60mm (bottom middle), 70mm (bottom right)

As explained earlier the air in the core of the spray is opposite in directions at 40mm and 60 mm and when the gas being pushed downwards and the air being sucked upwards hit each other a stagnation point is created and thus a radial flow is generated causing the spray to bend. This is visible in the figure 8 (bottom left) at 50 mm downstream where there is a ring of gas pushing outwards produced by the interactions of opposite gas

velocity in the core of spray cone. This radial flow is relatively larger than the air entrainment from outside the spray cone. Hence this radial flow blocks the air from the outer region of the spray cone completely and causes the spray plumes to bend from their original path. As expected at 70mm downstream position the radial velocity is a projection of the air entrained in the spray, with a large external recirculation around the jets – the process of jet-to-jet interaction is finished and the jets propagates linked to its previous (bent) direction.

Conclusions:

Numerical results with standard spray models and AMR approach show a good agreement for the both 3 and 6-hole GDI injectors compared to high-speed Mie scattering, PDA and PIV experimental data which have been performed in non-evaporating and evaporating conditions. The droplet size comparison between the experiments and numerical results at the center of the spray plume reveals a difference of less than 1μm in D_{10}. PDF of droplet distribution shows a good agreement. The penetration and vector fields of air entrainment for both injectors are very well captured. The air entrainment effects on the spray jets are observed and appear to be very pronounced. Jet to jet interaction appears to be linked with the reorganization of the flow due to the compact geometry. The narrow spray cone angle causes the air near the nozzle to be pushed downwards. This phenomenon occurs continuously during the spray propagation. The air which is pushed downwards doesn't allow the spray cone to expand until this air interacts with the air opposite in direction which is entrained from the lower region of the spray. The interactions of both positive and negative velocities result in outward radial velocity, which makes the spray plumes to deflect from their original path. At the deflection point a ring of vapor appears which is pushed along with the radial flow from the centre of the spray cone. The cone deflection angle in the simulations is measured roughly to be between 6° to 9°.

Acknowledgements

This work has been financially supported by the French Government within the framework of the FUI Magie project. The PDA measurements were supported by the excellence grant of Continental to Loughborough University.

References

[1] Rotondi R., Hélie J., Leger C., Mojtabi M., Wigley G., *ILASS Europe, Czech Republic, (2010).*

[2] Befrui B., Corbinelli G., D'Onofrio M., Varble D., *SAE Paper, 2011-01-1211, (2011).*

[3] Prosperi B., Helie J., Bazile R., *ILASS – Europe, Turkey, (2007).*

[4] Delay G., Bazile R., Charnay G., Nuglisch, H. J., *12th International Symposia on Applications of Laser Techniques to Fluid Mechanics, Portugal, (2004).*

[5] Seibel C., Gartung K., Arndt S., Weigand B., *ICLASS, Italy, (2003).*

[6] Skogsberg M., Dahlander P., Lindgren R., and Denbratt, I., *SAE Paper, 2005-01-0097, (2005).*

[7] Wigley G., Pitcher G., Nuglisch H., Helie J., Ladommatos N., *AVL 8th International Symposium on Combustion Diagnostics, Baden-Baden, Germany (2008).*

[8] Le Coz J-F., Lemenand C., Bruneaux G., *SAE paper, 2003-01-3108, (2003).*

[9] Bruneaux G., Causse M., Omrane A., *SAE paper, 2011-01-1828, (2011).*

[10] Malbec L-M., Bruneaux G., SAE paper, *2010-01-0342, SAE Int. J. Engines, 3(1):107-123, (2010).*

[11] Weller H., Tabor G., Jasak H., Fureby C., *J Comput Phys, 12(6):620–31, (1998).*

[12] Kosters A., "*Dynamic mesh refinement in dieselFoam*", *CFD with OpenSource software, project report, Division of Combustion, Chalmers University of Technology (2010).*

[13] Issa R., *J Comput Phys; 62:40–65, (1986).*

[14] Hestens M., Steifel E., *J Res Nat Bur Stand, 29:409–36, (1952).*

[15] Tanner F.X., *SAE Transactions Journal of Engines, 106 (3): 127-140, (1998).*

[16] O'Rouke P. J., *J. Comput. Physics, 83(2), 345–360,* (1989).

[17] Dukowitz J. K., *J. Comput. Physics, 35, 229, (1980).*

[18] Macpherson G. B., Nordin N., Weller H. G., *Commun. Numer. Meth. Engg; 25:263–273,* (2009).

[19] O'Rourke, P. J., "Collective Drop Effects on Vaporizing Liquid Sprays". *PhD thesis, Princeton University, (1981).*

[20] Karrholm F. P., "Numerical Modeling of Diesel Spray Injection, Turbulence Interaction and Combustion". *PhD thesis, Chalmers University of Technology, (2008).*